1999-11-01

Accuracy of scatterometer-derived winds using the Cramer-Rao bound

David G. Long
david_long@byu.edu

Travis E. Oliphant

Original Publication Citation
Oliphant, T. E., and D. G. Long. "Accuracy of Scatterometer-Derived Winds using the Cramer-Rao Bound." Geoscience and Remote Sensing, IEEE Transactions on 37.6 (1999): 2642-52

Accuracy of Scatterometer-Derived Winds using the Cramér–Rao Bound

Travis E. Oliphant and David G. Long, *Senior Member, IEEE*

***Abstract*— A wind scatterometer makes measurements of the normalized radar-backscatter coefficient σ° of the ocean surface. To retrieve the wind, a geophysical model function (GMF), which relates σ° to the near-surface wind, is used. The wind vector can be estimated using maximum-likelihood techniques from several σ° measurements made at different azimuth angles. The probability density of the measured σ° is assumed to be Gaussian with a variance that depends on the true σ° and therefore, depends on the wind through the GMF. With this model for wind estimation, the Cramér–Rao (C–R) bound is derived for wind estimation, and its implications for wind retrieval are discussed. As part of this discussion, the role of geophysical modeling error is considered and shown to play a significant role in the performance of near-surface wind estimates. The C–R bound is illustrated using parameters from the ERS AMI, NSCAT, and SeaWinds scatterometers.**

I. Introduction

SCATTEROMETERS have been used to estimate wind over the Earth's oceans from normalized radar cross-section (σ°) measurements since the successful flight of Seasat in 1978 [12]. Estimation is possible using the relationship between σ° and wind velocity given by an empirically-derived geophysical model function (GMF). This relationship does not generally admit selection of a single wind vector as the estimate due to inherent near-symmetry in the GMF. As a result, wind retrieval is typically a two-step process. First, a collection of wind vectors is estimated for each resolution element (or cell) using a traditional retrieval method such as least-squares or maximum-likelihood. Each of these possible wind solutions is called an *ambiguity* or an *alias* and is fed to a second step called *ambiguity removal* or *dealiasing*, which selects a single wind vector for each cell. The ambiguities have similar windspeed but differ in direction [12].

With any estimator, it is important to have a measure of the uncertainty in the estimate. Previous investigators have used simulations and comparisons with surface-wind data to report quality in wind estimates [2]. While useful for pre-flight scatterometer design, simulations require a significant number of computations, which somewhat limits their application. Using surface-wind data from buoys, ships, or island weather stations to assess wind-retrieval accuracy has its own difficulties, including limited cover and difficulty comparing surface-wind data to scatterometer-derived winds. Neither method is well-suited to delivering confidence estimates along with the retrieved wind for each cell where the wind is retrieved.

In this paper, we present the Cramér–Rao (C–R) bound as a measure of wind-retrieval accuracy that is useful for both scatterometer design and in-flight wind-retrieval assessment on a cell-by-cell basis. This measure allows useful evaluation of the accuracy of scatterometer-derived winds. The C–R bound provides a lower bound on the wind-estimate performance for parameter-estimation algorithms [4]. We apply this measure to the ERS-1/2 AMI scatterometer [1] and the NASA Scatterometer (NSCAT) [12]. In addition, we demonstrate the utility of the C–R bound in assessing scatterometer design by applying the technique to the predicted retrieval geometry of the SeaWinds scatterometer to be launched in 1999 [14].

The organization of this paper is as follows. First, we present a useful statistical model for scatterometer measurements, which incorporates geophysical-modeling error in a simplified fashion. The C–R bound for scatterometer wind retrieval is then derived as an approximation to the covariance of retrieved winds. The bound is then applied to ERS-1 and NSCAT data as a prediction of the statistical uncertainty in winds derived from these instruments. Finally, the bound is used to predict the effect on wind-retrieval accuracy of the new pencil-beam design to be used on the SeaWinds scatterometer.

II. Scatterometer-Measurement Model

To better understand the accuracy of the wind estimate, the C–R bound can provide a useful tool, since it gives the minimum achievable variance based on the assumed statistical model for the measurements. In this paper, we derive the C–R bound for scatterometer wind retrieval. Since the C–R bound depends on the statistical model, the scatterometer-measurement model is briefly presented.

One of the most important factors in determining a reliable statistically-based error estimate for retrieved winds is the statistical model for the noise in the measurements. Previous retrieval algorithms focus primarily on the noise due to instrumentation and background radiation [2], [12]. This implicitly assumes that the GMF, which relates wind velocity to normalized radar cross section, σ°, is an exact relationship. However, wind velocity is not the only factor affecting σ°. Other factors, such as local salinity, temperature, and long waves can change the observed σ° for a fixed wind vector. A statistical model for wind estimation, from which an analysis of error is desired, should account for this variability in the GMF.

Manuscript received July 11, 1997; revised October 28, 1998.

The authors are with the Department of Electrical Engineering, Brigham Young University, Provo, UT 84602 USA (e-mail: long@ee.byu.edu).

Publisher Item Identifier S 0196-2892(99)06143-4.

Let $\mathcal{M}(\theta, \psi - \phi, U, p)$ represent the GMF for a given frequency, where θ is the radar-incidence angle, ψ is the radar-azimuth angle, ϕ is the wind direction (measured from the same reference as ψ), U is the windspeed, and p is the radar polarization. In theory, this represents the mean of σ° observed under identical wind conditions. Associated with the GMF is the variance of σ° for the same identical wind conditions, instrument measurement noise not included. In principle, this variance, which we denote as $\mathcal{V}(\theta, \psi - \phi, U, p)$, accounts for the unmodeled (or unknown) parameters in relating wind velocity to σ°. Lacking a better statistical model for the variability, we assume the variation to be Gaussian. Then, for a particular set of $\theta, \chi(= \psi - \phi), U$ and p, the true normalized radar cross section σ_t° is modeled as a Gaussian random variable with mean $\mathcal{M}$ and variance $\mathcal{V}$. Defining

$$K_{pm} = \frac{\sqrt{\mathcal{V}}}{\mathcal{M}}$$

we write

$$\sigma_t^\circ = (1 + K_{pm} v_1)\mathcal{M}$$

where v_1 is a unit-variance, zero-mean random variable [8].

With this model, for the true σ° of the ocean surface, a scatterometer measurement z can be modeled as [2]

$$z = (1 + K_{pc} v_2)\sigma_t^\circ = (1 + K_{pc} v_2)(1 + K_{pm} v_1)\mathcal{M}$$

where v_2 is a unit-variance, zero-mean random variable independent of v_1, and K_{pc} is the normalized standard deviation of communication noise often represented as [7], [12]

$$K_{pc} = \sqrt{\alpha + \frac{\beta}{\sigma_t^\circ} + \frac{\gamma}{\sigma_t^{\circ 2}}}.$$

Here, α, β, and γ represent parameters in the noise model that are instrument dependent but independent of wind velocity [2], [12]. The statistics of the measurement z are difficult to compute, since K_{pc} is a function of σ_t°, which is unknown for real measurements. For typical values of β and γ, approximating σ_t° by its mean, $\mathcal{M}(\boldsymbol{w})$ in the equation for K_{pc} has little effect on the distribution of z [13]. Even with this approximation, z is the product of two Gaussian random variables whose distribution has complicated expresssion but near-Gaussian shape. As a result, approximating the distribution of z as Gaussian has little impact on wind retrieval [13]. Thus, we write the distribution of z, given the true wind vector $\boldsymbol{w}$, as

$$p_z(z|\boldsymbol{w}) = \frac{1}{\sqrt{2\pi}\varsigma(\boldsymbol{w})} \exp\left\{-\frac{[z - \mu(\boldsymbol{w})]^2}{2\varsigma^2(\boldsymbol{w})}\right\}$$

where E denotes expectation with

$$\mu(\boldsymbol{w}) = \mathrm{E}[z] = \mathcal{M}(\boldsymbol{w}),$$
$$\varsigma^2(\boldsymbol{w}) = \mathrm{Var}[z] = (K_{pc}^2 + K_{pm}^2 + K_{pc}^2 K_{pm}^2)\mathcal{M}^2(\boldsymbol{w}).$$

Wind retrieval requires two or more measurements from different azimuth angles [2], [12]. Lacking correlation information for K_{pm}, we model these measurements as independent so the measurement vector $\boldsymbol{z}$ is multivariate-Gaussian with diagonal covariance matrix. The mean of this measurement vector is comprised of the GMF evaluated at the true wind velocity, using the radar information associated with each measurement. We denote this measurement vector as $\mathcal{M}(\boldsymbol{w})$. The maximum-likelihood [4] wind estimate is then

$$\hat{\boldsymbol{w}} = \boldsymbol{h}(z) = \arg\max_{\boldsymbol{w}}[\log p_{\boldsymbol{z}}(\boldsymbol{z}|\boldsymbol{w})]. \quad (1)$$

Typically, the likelihood function has multiple significant maxima, which implies several wind-vector estimates. This makes it difficult to talk about the statistics of the wind estimate until after ambiguity removal has been performed to select a single wind estimate. Trying to account for the ambiguity-removal step in a complete statistical development of the wind estimate is difficult given the *ad hoc* nature of most ambiguity-removal algorithms.

Instead, we ignore the ambiguity removal and focus attention on the wind ambiguities. Each of the ambiguities is a function of the random measurements and is therefore a random vector. By approximating the covariance of each ambiguity and then assuming the ambiguity-removal algorithm selects the ambiguity corresponding to the true wind, a reliable covariance will be selected as well. While this does not convey the complete picture since ambiguity selection is ignored, it does provide a quantitative measure of how sensitive each individual ambiguity is to the noisy measurements. With this

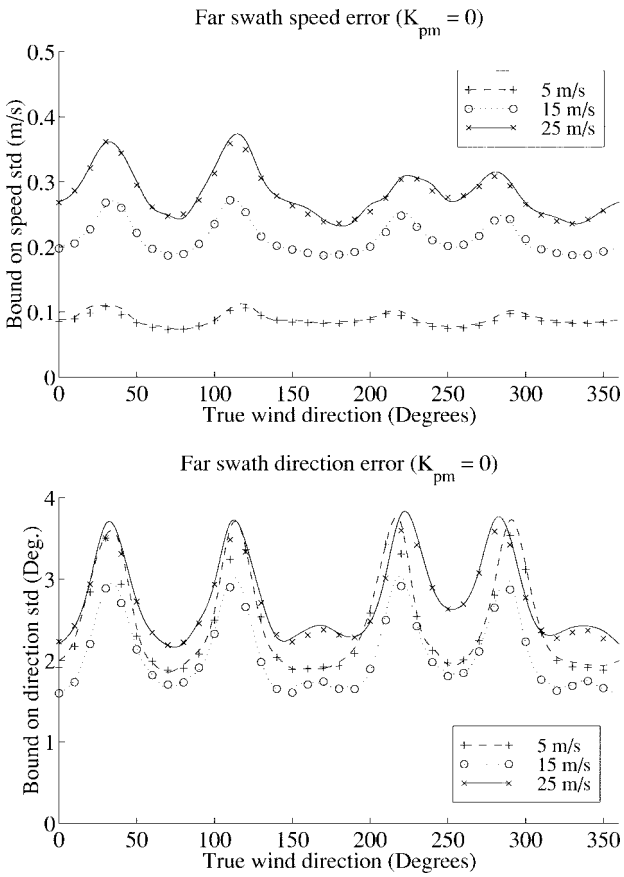

Fig. 1. Unbiased C–R bound and simulation-computed standard deviations for various windspeeds and wind directions at far swath for the ERS-1 geometry and noise variance, with $K_{pm} = 0$ using the CMOD4 GMF. The markers are the C–R-bound calculation, and the curves are sinc-interpolated simulation results.

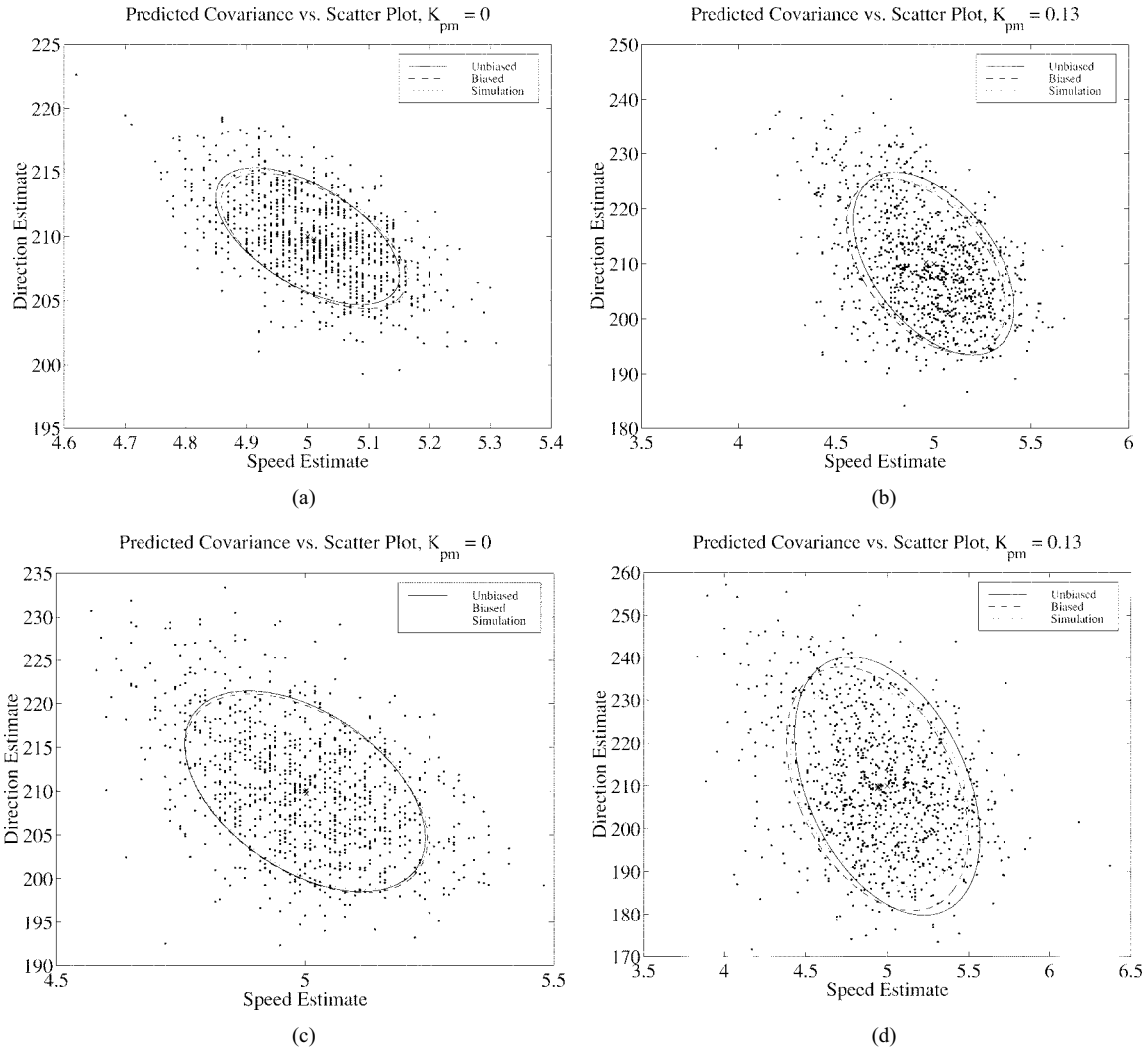

Fig. 2. ERS-1 simulation scatter plots compared with C–R bounds using the CMOD4 GMF. Each point represents the result of a wind retrieval from a Monte Carlo simulation. One thousand wind retrievals were done for each plot. Ellipses represent 70% bounds assuming a two-dimensional (2-D) Gaussian distribution.

in mind, we proceed to approximate the covariance of each wind ambiguity using the C–R lower bound.

III. Cramér–Rao Bound

The C–R bound gives a lower bound on the covariance of any unbiased estimator [4]. This bound has been generalized to the case of any estimator (biased or unbiased) [3]. While the wind estimate is generally unbiased, it can be biased for some wind directions. Thus, both bounds will be computed and compared to simulations.

The general C–R bound can be expressed, using E as the expectation operator over the measurements $\boldsymbol{z}$, as [4]

$$\begin{aligned}\boldsymbol{C}(\boldsymbol{w}) &= E\{[\hat{\boldsymbol{w}} - E\hat{\boldsymbol{w}}][\hat{\boldsymbol{w}} - E\hat{\boldsymbol{w}}]^T\} \\ &\geq \frac{\partial E\hat{\boldsymbol{w}}}{\partial \boldsymbol{w}} \boldsymbol{J}^{-1}(\boldsymbol{w}) \frac{\partial E\hat{\boldsymbol{w}}^T}{\partial \boldsymbol{w}}\end{aligned}$$

where $\boldsymbol{J}(\boldsymbol{w})$ is the Fisher-information matrix defined as

$$\boldsymbol{J}(\boldsymbol{w}) = E\left\{\left[\frac{\partial L(\boldsymbol{w},\boldsymbol{z})}{\partial \boldsymbol{w}}\right]^T \frac{\partial L(\boldsymbol{w},\boldsymbol{z})}{\partial \boldsymbol{w}}\right\}.$$

In this expression, L is the log-likelihood function

$$L(\boldsymbol{w},\boldsymbol{z}) = \log p_{\boldsymbol{z}}(\boldsymbol{z}|\boldsymbol{w})$$

and the vector derivative is a row operator. If $E\hat{\boldsymbol{w}} = \boldsymbol{w} + \boldsymbol{a}$, where $\boldsymbol{a}$ is an arbitrary constant vector, we obtain the unbiased C–R bound[1]

$$\boldsymbol{C} \geq \boldsymbol{J}^{-1}.$$

Using the measurement model described in the previous section, it can be shown that with K measurements in $\boldsymbol{z}$,

$$J_{ij} = \sum_{k=1}^{K} \left[\frac{\partial \mathcal{M}_k}{\partial w_i} \frac{1}{\varsigma_k^2} \frac{\partial \mathcal{M}_k}{\partial w_j} + \frac{\partial \varsigma_k^2}{\partial w_i} \frac{1}{2\varsigma_k^4} \frac{\partial \varsigma_k^2}{\partial w_j}\right] \qquad (2)$$

where $\partial \mathcal{M}_k / \partial w_i$ is the partial derivative of the GMF evaluated at $\boldsymbol{w}$ with respect to wind component w_i [13]. The subscript k implies the model function is evaluated with azimuth angle, incidence angle, and polarization determined

[1] To reflect its range of validity more accurately, it should be termed the constant-biased C–R bound. However, we stick to more common terminology and call it the unbiased C–R bound

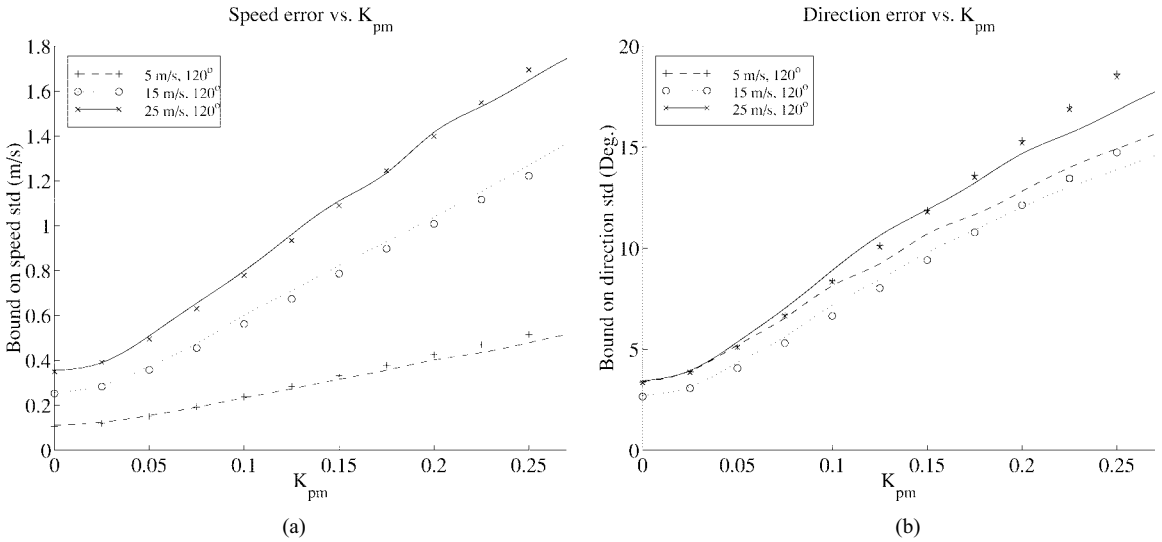

Fig. 3. C–R lower bound on ERS-1 speed and direction-error standard deviation versus K_{pm} for far swath location. Markers are the bound and curves are sinc-interpolated simulation results.

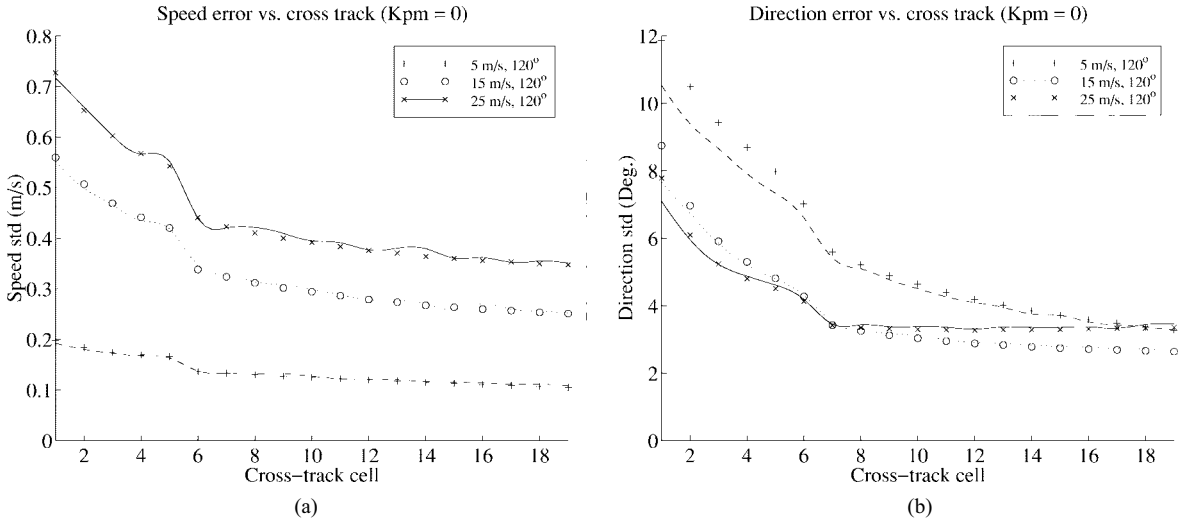

Fig. 4. C–R Lower bound on ERS-1 speed and direction-error standard deviation versus cross-track cell location for $K_{pm} = 0$. Markers are the bound and curves are sinc-interpolated simulation results.

by the kth measurement in $\boldsymbol{z}$. The variance of the kth measurement is denoted in this equation as ς_k^2. Its derivative with respect to w_i can be expressed as

$$\frac{\partial \varsigma_k^2}{\partial w_i} = [2\epsilon_k \mathcal{M}_k + \beta_k(1 + K_{pm}^2)]\frac{\partial \mathcal{M}_k}{\partial w_i}$$

where

$$\epsilon_k = \alpha_k(1 + K_{pm}^2) + K_{pm}^2.$$

The partial derivatives of the GMF are typically obtained numerically and can be computed for polar $\boldsymbol{w} = (U, \phi)$ or rectangular $\boldsymbol{w} = (u, v)$ coordinates. In this paper, a polar-coordinate system is assumed with the angle measured clockwise from geographical north.

Computing the biased C–R bound is generally difficult, since there is no explicit formula for the bias. In order to determine the biased C–R bound, we adopt the approach discussed by Fessler [5] to approximate the bias. We expand the implicit function defined in (1) by a first-order Taylor series about the mean of the measurements $\overline{\boldsymbol{z}} = \mathcal{M}(\boldsymbol{w})$ and then calculate the expected value of this expansion. The result is

$$\begin{aligned} E\hat{\boldsymbol{w}}(\boldsymbol{w}) &\approx \arg\max_{w} [\log p_{\boldsymbol{z}}(\mathcal{M}(\boldsymbol{w})|w)] \\ &= \boldsymbol{h}(\mathcal{M}(\boldsymbol{w})). \end{aligned}$$

Note that $\boldsymbol{h}(\mathcal{M}(\boldsymbol{w}))$ is wind retrieval performed on the noiseless σ° measurement vector $\mathcal{M}(\boldsymbol{w})$. The gradient of the bias can be approximated as the gradient of the previous equation. Using the chain rule

$$\frac{\partial E\hat{\boldsymbol{w}}}{\partial \boldsymbol{w}} = \left.\frac{\partial \boldsymbol{h}(\boldsymbol{z})}{\partial \boldsymbol{z}}\right|_{\boldsymbol{z}=\mathcal{M}(\boldsymbol{w})} \frac{\partial \mathcal{M}(\boldsymbol{w})}{\partial \boldsymbol{w}} = \boldsymbol{D}(\boldsymbol{w})\boldsymbol{G}(\boldsymbol{w})$$

where

$$\boldsymbol{G}(\boldsymbol{w}) = \frac{\partial \mathcal{M}(\boldsymbol{w})}{\partial \boldsymbol{w}}$$

is a $K \times 2$ matrix (which can be numerically approximated) and

$$\boldsymbol{D}(\boldsymbol{w}) = \left.\frac{\partial \boldsymbol{h}(\boldsymbol{z})}{\partial \boldsymbol{z}}\right|_{\boldsymbol{z}=\bar{\boldsymbol{z}}=\mathcal{M}(\boldsymbol{w})}$$

which is a $2 \times K$ matrix, computed using the chain rule as described by Fessler [5]

$$\boldsymbol{D}(\boldsymbol{w}) = -[\boldsymbol{D}^{20}(\boldsymbol{w})]^{-1}\boldsymbol{D}^{11}(\boldsymbol{w}).$$

$\boldsymbol{D}^{20}$ is the 2×2 Hessian of the log-likelihood function (for fixed $\boldsymbol{z}$), while $\boldsymbol{D}^{11}$ is the $2 \times K$ matrix of mixed-derivatives of the log-likelihood function. The elements of $\boldsymbol{D}^{11}$ and $\boldsymbol{D}^{20}$ are given expressly, using previously defined symbols, as

$$\begin{aligned}
D_{ij}^{11} &= \frac{\partial^2 L(\boldsymbol{w},\boldsymbol{z})}{\partial w_i \partial z_j}, \\
&= \frac{1}{\tilde{\varsigma}_j^2}\frac{\partial \tilde{\mathcal{M}}_j}{\partial w_i} + \frac{\mathcal{M}_j - \tilde{\mathcal{M}}_j}{\tilde{\varsigma}_j^4}\frac{\partial \tilde{\varsigma}_j^2}{\partial w_i}, \\
D_{ij}^{20} &= \frac{\partial^2 L(\boldsymbol{w},\boldsymbol{z})}{\partial w_i \partial w_j}, \\
&= \sum_{k=1}^{K}\left[-\frac{\partial \tilde{\mathcal{M}}_k}{\partial w_i}\frac{1}{\tilde{\varsigma}_k^2}\frac{\partial \tilde{\mathcal{M}}_k}{\partial w_j} + \frac{\partial \tilde{\varsigma}_k^2}{\partial w_i}\frac{1}{2\tilde{\varsigma}_k^4}\frac{\partial \tilde{\varsigma}_k^2}{\partial w_j}\right. \\
&\quad - \frac{1}{2\tilde{\varsigma}_k^2}\frac{\partial^2 \tilde{\varsigma}_k^2}{\partial w_j} \\
&\quad - \frac{\mathcal{M}_k - \tilde{\mathcal{M}}_k}{\tilde{\varsigma}_k^4}\left(\frac{\partial \tilde{\mathcal{M}}_k}{\partial w_i}\frac{\partial \tilde{\varsigma}_k^2}{\partial w_j} + \frac{\partial \tilde{\mathcal{M}}_k}{\partial w_j}\frac{\partial \tilde{\varsigma}_k^2}{\partial w_i}\right) \\
&\quad + \frac{\mathcal{M}_k - \tilde{\mathcal{M}}_k}{\tilde{\varsigma}_k^2}\frac{\partial^2 \tilde{\mathcal{M}}_k}{\partial w_j \partial w_i} \\
&\quad - \frac{\partial \tilde{\varsigma}_k^2}{\partial w_i}\frac{(\mathcal{M}_k - \tilde{\mathcal{M}}_k)^2}{\tilde{\varsigma}_k^6}\frac{\partial \tilde{\varsigma}_k^2}{\partial w_j} \\
&\quad \left. + \frac{(\mathcal{M}_k - \tilde{\mathcal{M}}_k)^2}{2\tilde{\varsigma}_k^4}\frac{\partial^2 \tilde{\varsigma}_k^2}{\partial w_j \partial w_i}\right]
\end{aligned}$$

where

$$\begin{aligned}
\frac{\partial^2 \tilde{\varsigma}_k^2}{\partial w_i \partial w_j} &= [2\epsilon_k \tilde{\mathcal{M}}_k + \beta_k(1 + K_{pm}^2)]\frac{\partial^2 \tilde{\mathcal{M}}_k}{\partial w_i \partial w_j} \\
&\quad + 2\epsilon_k \frac{\partial \tilde{\mathcal{M}}_k}{\partial w_i}\frac{\partial \tilde{\mathcal{M}}_k}{\partial w_j}, \\
\frac{\partial \tilde{\varsigma}_k^2}{\partial w_i} &= [2\epsilon_k \tilde{\mathcal{M}}_k + \beta_k(1 + K_{pm}^2)]\frac{\partial \tilde{\mathcal{M}}_k}{\partial w_i}
\end{aligned}$$

and $\tilde{M}_k = \mathcal{M}_k(\boldsymbol{h}(\bar{\boldsymbol{z}}))$. Similar notation for the partial derivatives of $\mathcal{M}_k$ emphasize that they are evaluated at $\boldsymbol{h}(\bar{\boldsymbol{z}}) = \boldsymbol{h}(\mathcal{M}(\boldsymbol{w}))$.

It should be emphasized that the computation for the biased bound given here is only an approximation and has two significant limitations. First, the linear approximation used to compute the mean may not always be adequate to compute the gradient of the mean. In principle, a higher-order Taylor series could be used to improve the approximation. This would require third-order and fourth-order derivatives of the GMF, which are difficult to obtain accurately from a tabular GMF. Second, the derivative matrix $\boldsymbol{D}^{20}$ may be nearly singular for some wind directions and measurement geometries. This can lead to significant sensitivity to the method used to compute the derivatives when estimating the biased C–R bound. Nonetheless, the approximation outlined here (which was adapted from a more detailed discussion in Fessler in [5]) is useful in improving the covariance estimate for certain wind directions where the retrieval process is biased, and the unbiased C–R bound does not approximate the simulated covariance well.

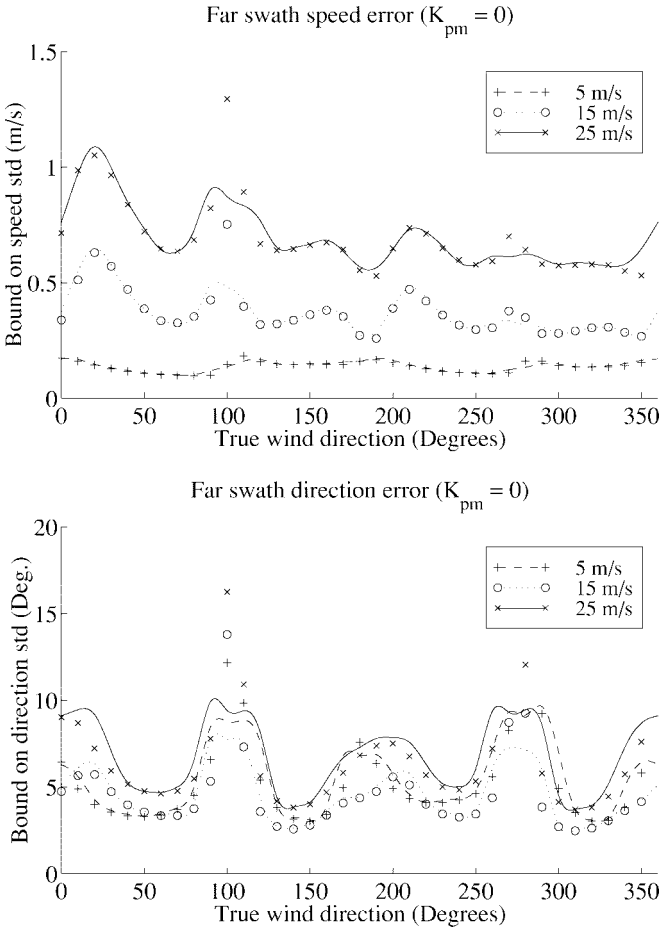

Fig. 5. Unbiased C–R bound for various windspeeds and wind directions at far swath for the NSCAT geometry and noise variance with $K_{pm} = 0$, using the NSCAT1 GMF. Markers are the C–R bound, and curves are sinc-interpolated simulation results.

As a lower bound on the estimate performance, the C–R bound is useful in evaluating wind retrieval both as a reporting tool and a design tool. It also can be a useful measure of the covariance of a given wind estimate and as an uncertainty measure of the retrieved wind when assimilating scatterometer wind measurements into global-circulation models. As the actual bound depends on the true wind vector (which is unavailable), the C–R-bound covariance must be reported approximately by assuming that the retrieved wind is the true wind vector. In simulations or during design in which the true wind is known, the C–R bound can be reported correctly.

In the next two sections, the retrieval precision of ERS-1/2 and NSCAT are evaluated using the C–R bound. The C–R bound is also useful as a design tool in obtaining predictions of scatterometer performance. The final section uses the bound to give predictions of the accuracy of the

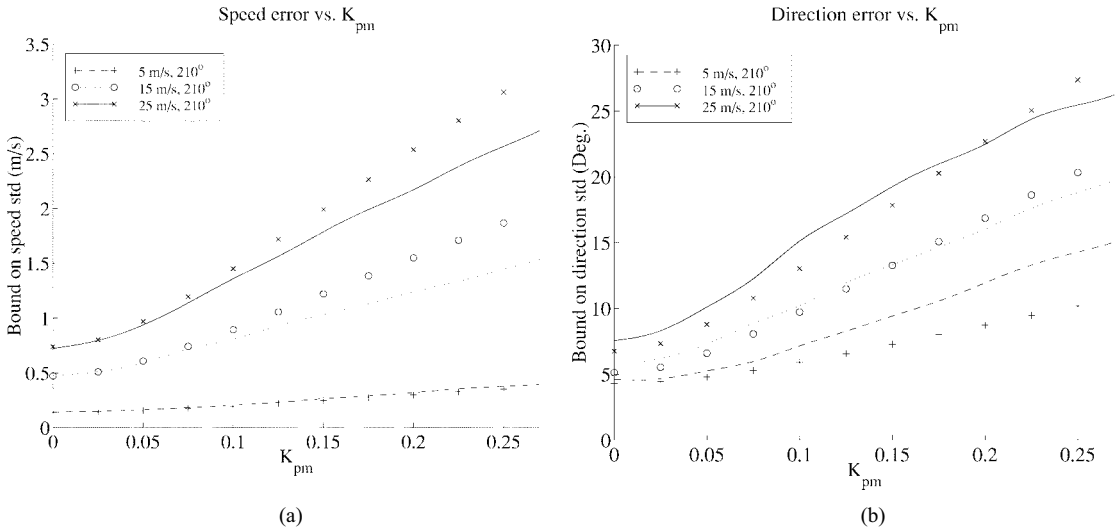

(a) (b)

Fig. 6. C–R lower bound on-speed and direction-error standard deviation versus K_{pm} for NSCAT far-swath location.

SeaWinds scatterometer. In all three sections, the predicted covariance is compared to simulation in order to evaluate the usefulness of the C–R bound as a realistic measure of uncertainty.

IV. Cramér–Rao Bound for ERS-1/2

In this section, we evaluate the C–R bound for wind retrieval using ERS-1/2 AMI scatterometer measurements. The discussion is intended to be neither a validation of nor an exhaustive study of the performance of the ERS scatterometer. It is presented to illustrate the utility of the C–R bound in analyzing the wind-measurement performance.

In order to understand the results presented, a brief review of ERS-scatterometer geometry is instructive. A detailed description of the C-band ERS-1 scatterometer is given in [1]. The ERS-2 scatterometer is an identical follow-on instrument. Three beams obtain σ° measurements from each wind vector cell (WVC) at two incidence angles and three different azimuth angles. The measurement SNR is very high, so most of the noise in wind retrieval comes from the geophysical-modeling error (K_{pm}). There are nineteen WVC's across the single swath with $(K = 3)$ measurements from each WVC. Wind-retrieval geometry, and consequently wind-retrieval error, is distinct for each cell across the swath. For convenience, representative WVC's are selected for study. In the following, the European Space Angency (ESA) reported ERS-1 geometry, and noise variance along with the CMOD4 GMF [6] are used, though we have observed quite similar results with other GMF's.

V. Results

The unbiased C–R bound for a representative far swath wind-vector cell of ERS-1 as a function of the true windspeed and direction is plotted with markers in Fig. 1. The data for this figure were generated assuming no modeling error ($K_{pm} = 0$ and no uncertainty in the GMF). Note that both the wind-direction error and windspeed error are peaked at particular directions. While this behavior has been previously attributed to problems with using the correct model function in wind retrieval, the C–R bound suggests that this behavior is intrinsic to the wind-estimation problem. The larger variance at these directions can be attributed to the shape of the model function and the relative azimuth angles of the observations. When one of the fore or aft scatterometer beams is directly upwind or directly downwind, there is less information about the wind in the measurements [13].

For comparison, standard-deviation estimates from a simple compass simulation [2] with the maximum-likelihood (ML) wind-retrieval algorithm are also shown in Fig. 1 with the solid lines. For a given WVC, the compass simulation is performed by repeating the following steps N times: 1) calculating the GMF for each true wind vector; 2) adding noise according to the K_{pc} associated with that WVC and desired K_{pm}; 3) retrieving the wind by maximum-likelihood optimization; and 4) selecting the wind alias that is closest to the true wind as the simulated wind estimate. The N-retrieved winds are used to calculate statistics on the wind estimate. More details on compass simulation can be found in [2].

In Fig. 1, the curves were created by sinc-interpolation of simulation results. These lines appear to also interpolate the C–R bound results, suggesting that the wind-retrieval algorithm is statistically efficient in an estimation-theoretic sense at far swath and zero GMF error. For most ERS-1 WVC's and true wind velocities, the agreement between covariance predicted with the unbiased C–R bound and covariance calculated by simulations is excellent [13], as suggested by Fig. 2(a)–(d). These figures also show that the small disparity between the covariance estimated with the C–R bound and the simulated covariance that occurs at low windspeed and high K_{pm} values can be improved by using the biased C–R-bound approximation, although the effect is small in these cases.

We can use the C–R bound to investigate the sensitivity of wind estimation to other wind-retrieval conditions. In particular, Fig. 3 shows an example at a representative far swath WVC of the sensitivity of the wind estimate to the GMF normalized variance (K_{pm}) for several windspeeds and a direction of 120° (corresponding to an uncertainty peak). This

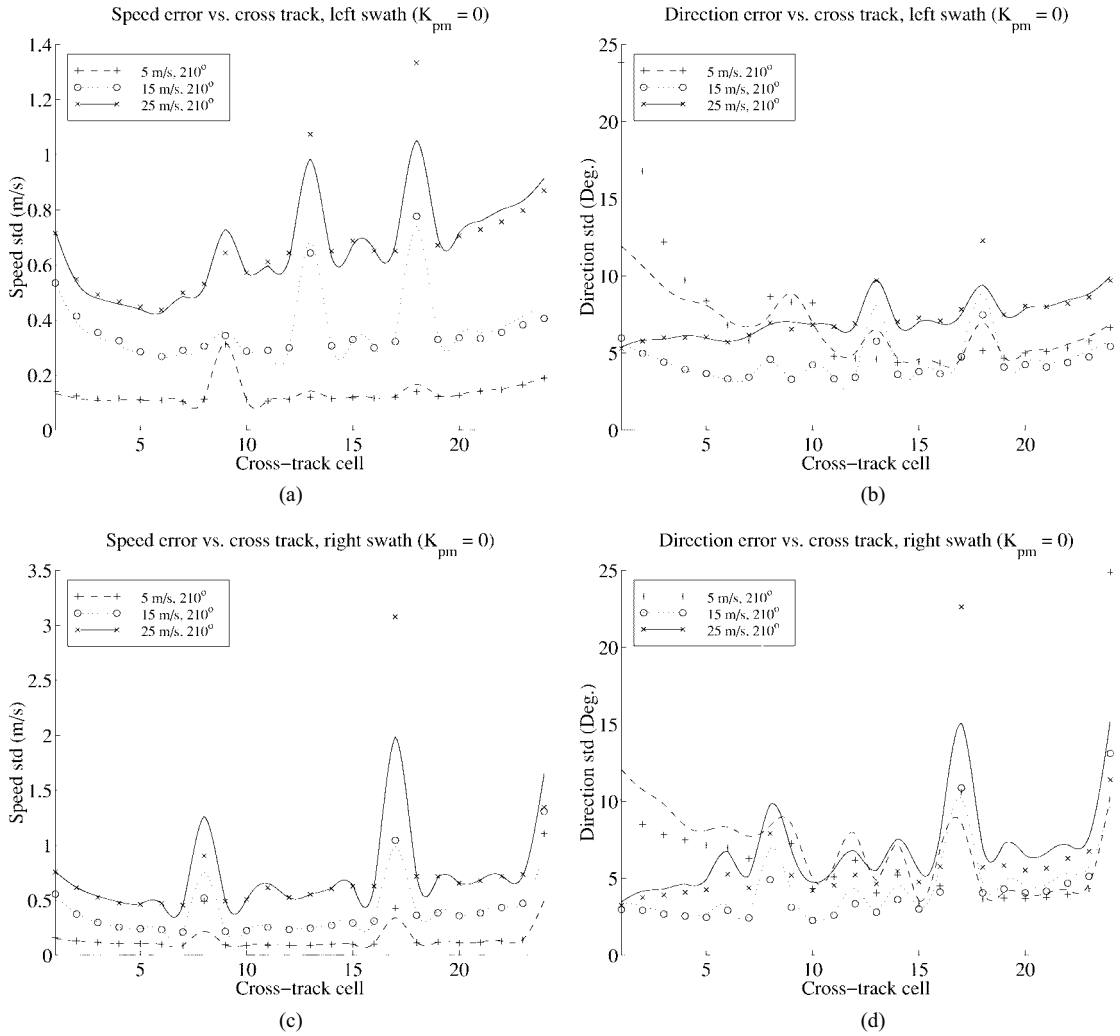

Fig. 7. C–R lower bound on-speed and direction-error standard deviation versus cross-track cell location for $K_{pm} = 0$.

figure suggests that the accuracy of wind estimates from ERS-1 data is quite sensitive to the precise value of K_{pm} (which is not well known). Again, in this figure, markers indicate the C–R-bound standard deviation, while the solid lines represent sinc-interpolations of simulated data. The comparison between simulations and the C–R bound shows good agreement except at high values of K_{pm} and low windspeeds, where the unbiased C–R bound overpredicts the simulated standard deviation in the wind-direction estimate. This indicates that under these conditions, the wind estimate is biased. The approximate biased C–R bound is closer to the simulated results, as in Fig. 2.

Another point of interest is the accuracy of wind estimates across the swath. Fig. 4 shows the C–R bound on the standard deviation of speed and direction estimates as the cross-track cell number varies from near (1) to far (19). The true wind direction for these plots is 120°, and the results for several windspeeds are shown. This figure shows quantitatively that near-swath winds are not as accurate, especially for low windspeeds. In addition, at near swath and under low windspeeds, the unbiased C–R bound over-predicts simulation performance, indicating a biased estimator under these conditions.

VI. Cramér–Rao Bound for NSCAT

In this section, we give results of the C–R bound applied to NSCAT-retrieved winds using representative NSCAT geometry and noise-data. As before, the discussion is not intended to be a validation of nor an exhaustive study of NSCAT performance, but is presented to illustrate the utility the C–R bound in analyzing the wind-measurement performance.

In order to more fully understand the results, a brief overview of NSCAT is helpful. A more detailed description is contained in [12]. The NSCAT instrument was launched in August 1996 aboard the Japanese satellite ADEOS. It operates under the same general principles as ERS-1 but with significant differences that contribute to different error characteristics. Three main factors contribute to differences in wind estimates from ERS-1 and NSCAT: operating frequency, transmit power, and measurement geometry. NSCAT operates in Ku-band at 14 GHz. As a result, the model function used to relate wind velocity to σ° is different from that used for ERS-1 data. One significant difference is that azimuth modulation is more pronounced at low windspeeds than at C-band, suggesting that wind-direction retrieval may be more accurate at lower windspeeds with NSCAT than with

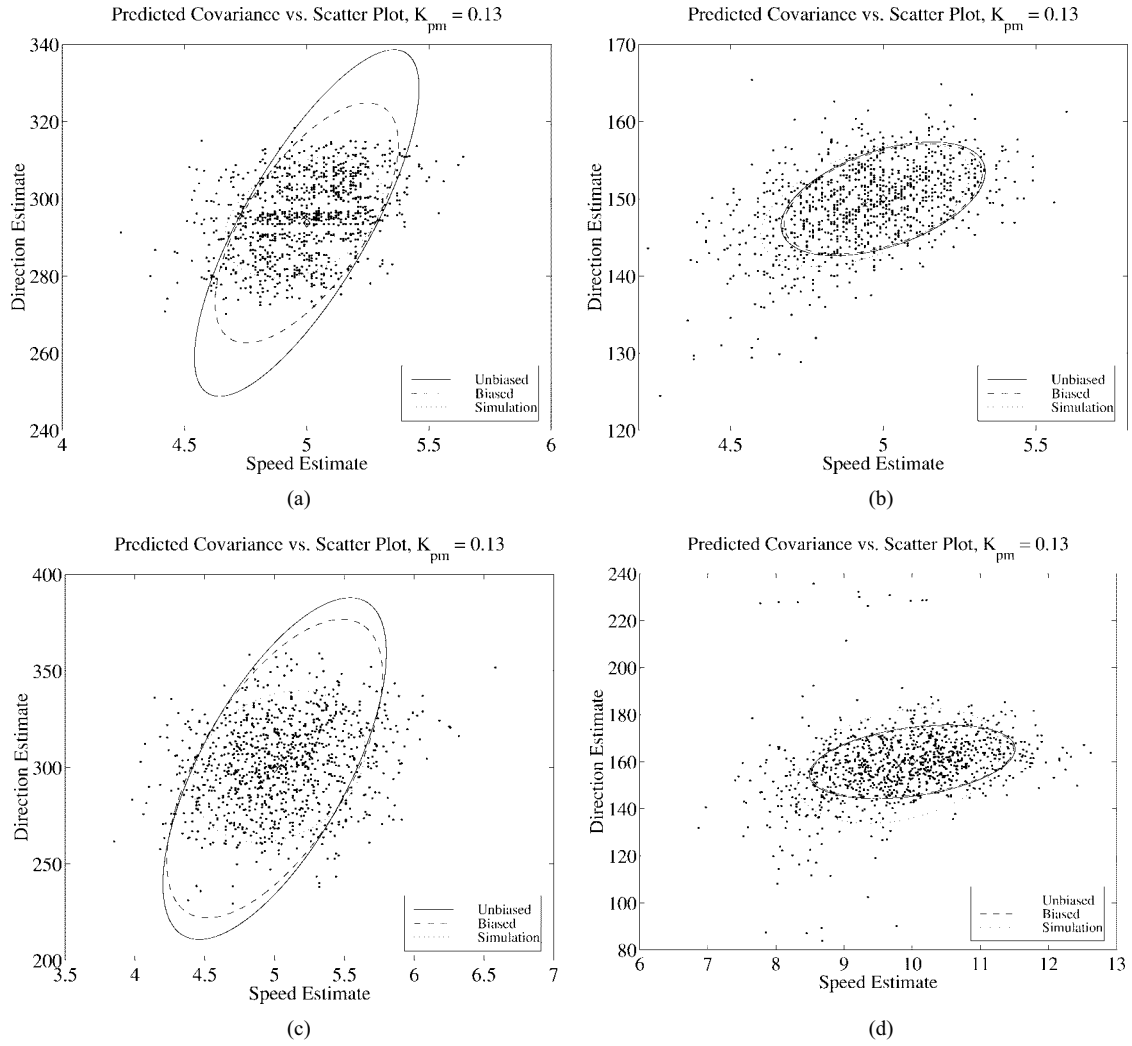

Fig. 8. NSCAT simulation scatter plots compared to C–R bounds using $K_{pm} = 0.13$ and the NSCAT1 GMF. Each point represents the result of a wind retrieval from a Monte Carlo simulation. Ellipses represent 70% bounds assuming a 2-D Gaussian distribution.

ERS-1 [9]. The C–R bound allows us to easily quantify this hypothesis for a specific WVC.

NSCAT uses 120-W peak-transmit power compared to about 5 kW for ERS-1. Consequently, the SNR of NSCAT data is lower, resulting in a larger value of K_{pc}. This does not necessarily mean NSCAT retrieves wind less accurately, however, as GMF modeling error plays a major role in the wind-retrieval precision.

A key difference between ERS-1 and NSCAT is retrieval geometry for the center antenna. NSCAT uses three beams on each side of the spacecraft to gather data for two swaths, each approximately 600-km across [12]. The fore and aft beams are separated by 90°, while the center beam is offset 25° from center to facilitate the use of Doppler processing. In addition, the center beam makes both horizontal and vertical-polarization measurements, while the fore and aft beams make vertical-polarization measurements only. Nominally sixteen measurements are gathered to estimate the wind in a 50-km square WVC. Each of the two swaths has 12 such cells. However, the measurements can also be collocated so that three to five measurements are available for each of 24–25-km resolution cells per swath. In the following, we use the NSCAT1 GMF [10], [11], although the results are similar for the Wentz [15] (SASS-2) GMF.

VII. Results

This section details a few results of applying the C–R bound to representative NSCAT WVC's. The unbiased C–R bound for a representative far swath WVC as a function of the true windspeed and direction is plotted in Fig. 5, assuming the modeling error is zero ($K_{pm} = 0$). As was the case for the ERS-1, both the wind-direction error and windspeed error are peaked at particular true wind directions. However, the asymmetric beam arrangement for NSCAT creates a larger peak in the direction of the fore or aft beam closest to the center beam.

For comparison, sinc-interpolated simulation results are also shown in Fig. 5 as curves. In the simulation, the wind error is for the ambiguity closest to the true wind direction. The C–R bound and simulation plots are close but not identical. As in ERS-1 at near-swath and low windspeeds, the large peak in wind-direction uncertainty predicted by the C–R bound for a true windspeed aligned with the fore or aft beam is

significantly reduced in the simulations. For NSCAT, however, this is only true when the true wind direction is closely aligned with the fore or aft beam nearest the center beam. The peak is lower in the simulation, because the wind estimate is biased at these locations. For all but these locations, the unbiased C–R bound gives uncertainty predictions that are very close to simulations. This suggests that the wind-estimation algorithm for NSCAT is statistically efficient in an estimation-theoretic sense for almost all wind directions. Similar results apply for near and mid-swath WVC's. These empirical results justify using the unbiased C–R bound as a predictor of the uncertainty whenever the retrieved wind is not aligned with the fore or aft beam closest to the NSCAT center beam.

In order to explore some of the predictions of the C–R bound for the NSCAT instrument, consider Figs. 6 and 7. These graphs show how wind-velocity uncertainty varies according to K_{pm} and cross-track location, as predicted by the C–R bound for the NSCAT instrument. We note that NSCAT predictions are also sensitive to the true value of K_{pm} over a wide range of K_{pm} values at 25-km resoultion. Also, when evaluating the cross-track plots, it should be kept in mind that some of the WVC's have only three measurements available, thus causing the variable-estimation performance at certain cross-track locations.

Fig. 8(a)–(d) shows worst-case and typical predictions made by the unbiased and biased C–R bound for near and far-swath WVC's. Visual inspection suggests that the unbiased C–R bound is a good bound for the typical case but is less accurate for the worst case. This is because the wind estimate is biased at these wind directions. While the approximation to the biased bound calculated in this paper improves the agreement between simulation and prediction, the approximation is not good enough to completely predict the biased-estimator performance.

VIII. Cramér–Rao Bound for SeaWinds

The previous two sections applied the C–R bound to predicting wind uncertainties for past or current scatterometers. This section applies the method to predicting wind uncertainties for the future SeaWinds scatterometer to be launched in 2000[2] [14]. While ERS-1/2 and NSCAT are fan-beam scatterometers, SeaWinds is based on a scanning pencil-beam design. SeaWinds uses a dual-beam, scanning pencil-beam antenna. The two antenna beams are at different incidence angles and sweep out two large circles on the ocean with radii of approximately 850 and 1100 km, respectively. As a result, the two to four azimuth measurements from each 25-km cell are at fixed incidence angles but have varying azimuthal relationships depending on the (cross-track) distance from the projected along-track of the satellite. This creates a retrieval geometry for SeaWinds that eliminates the nadir gap.

The effect of these geometries on wind retrieval can be explored with the C–R bound. Using this as a prediction of wind uncertainty allows insight into the wind-measurement of the performance of the SeaWinds design.

[2] An early copy of SeaWinds was successfully launched aboard QuikScat in June 1999. The results presented herein are prelaunch predictions.

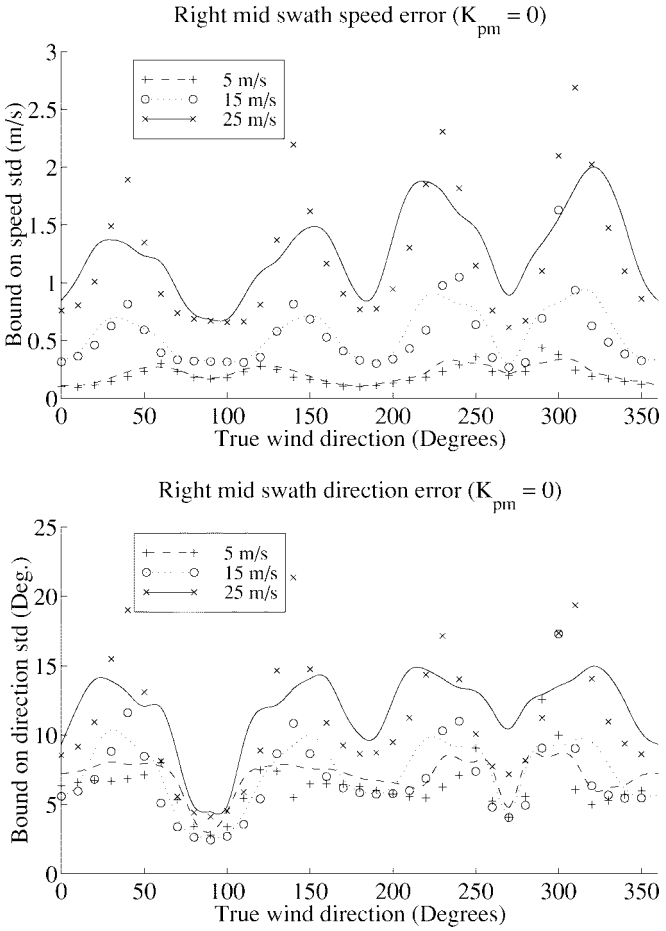

Fig. 9. Unbiased C–R bound (markers) and simulation (curves) calculated for several true windspeeds and directions. SeaWinds geometry and noise variance for a WVC 350 km to the right (facing in direction of satellite motion) from the subsatellite track are used, along with zero-modeling error and the NSCAT1 GMF. The curves are sinc-interpolated, simulated standard deviations. Wind direction is measured clockwise from direction of satellite motion.

Fig. 9 shows the predictions of the unbiased C–R bound using SeaWinds geometry and K_{pc} at 50-km resolution [14]. The NSCAT1 GMF with a $K_{pm} = 0$ is used. The results shown are for a mid-swath cell about 350 km to the right of the subsatellite track when facing the direction of satellite motion. As with the other instruments, the C–R bound agrees well with simulations for most true wind directions and windspeeds. As in the previous case, at the characteristic peaks in uncertainty, the unbiased C–R bound overpredicts the simulation result, because the wind estimate is biased at these wind velocities. Using the approximation to the biased C–R bound outlined in this paper improves the correspondence between prediction and simulation somewhat. Even though the C–R bound does not perfectly predict the wind-estimate covariance, this figure demonstrates that it can be a useful prediction of the uncertainty of retrieved wind for SeaWinds.

It is interesting to note that in the case of the SeaWinds instrument, the large peaks in retrieval uncertainty do not occur when the true wind is aligned with the measurement as was the case with the fixed azimuthal relationships in ERS-1 and NSCAT. Instead, the largest values in wind-retrieval

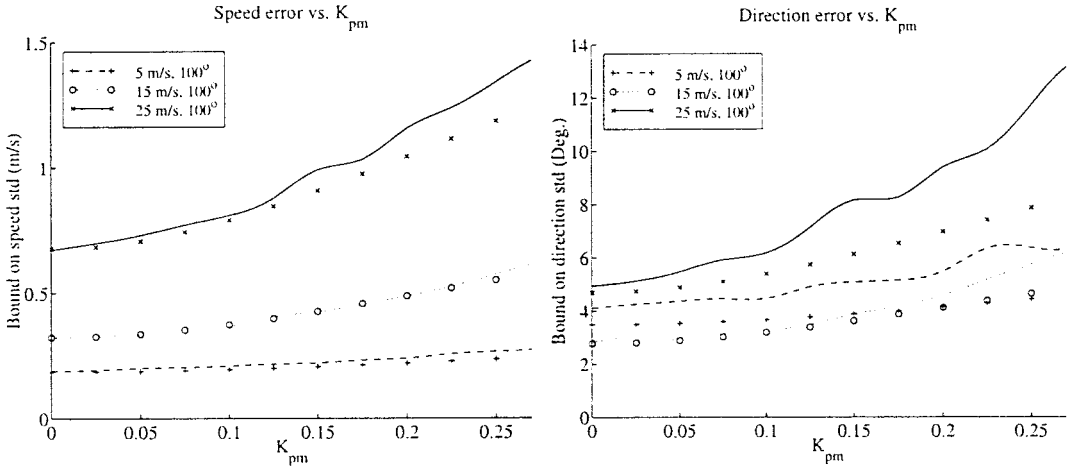

(a) (b)

Fig. 10. C–R lower bound on-speed and direction-error standard deviation versus K_{pm} for SeaWinds mid- and right-swath locations. Markers are unbiased C–R bounds and curves are sinc-interpolated simulations.

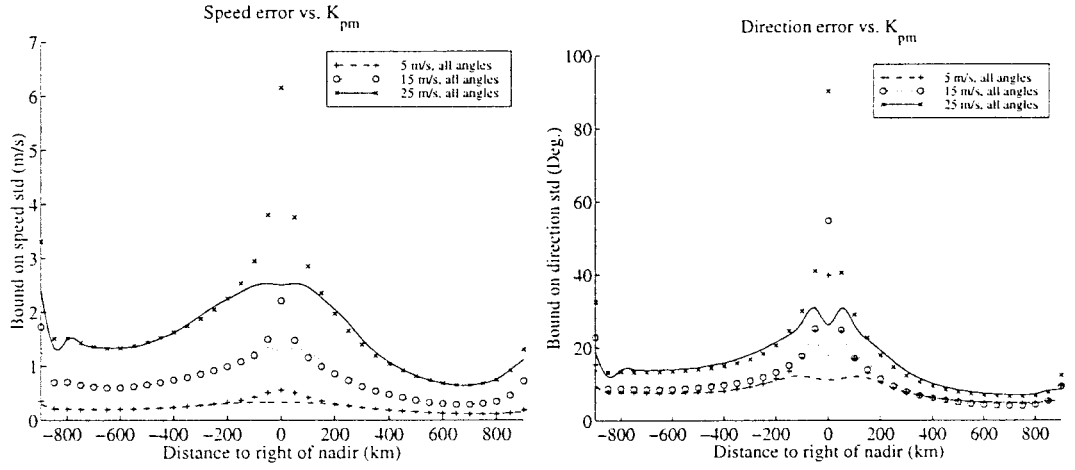

(a) (b)

Fig. 11. C–R Lower bound on-speed and direction-error standard deviation versus cross-track locations. Negative distances are left swath and positive distances are right swath. Markers are unbiased C–R bounds and curves are sinc-interpolated simulations.

uncertainty consistently occur when the true wind velocity is near 40, 140, 220, and 320 degrees clockwise form the direction of the satellite motion at this cross-track distance.

Fig. 10 shows the effect on wind-retrieval uncertainty of different values of K_{pm} as predicted by the unbiased C–R bound. The data for this figure was generated using a mid swath location with a true direction of 100° (near a valley). This figure suggests that uncertainty in wind retrieval using SeaWinds is sensitive to K_{pm}, though the sensitivity is less than for NSCAT.

Finally, Fig. 11 demonstrates use of the C–R bound to understand cross-track performance of the SeaWinds instrument. Also included in this figure are interpolated simulation results. There is generally good agreement between the simulated results and the C–R bound in this figure except for at isolated points where the wind estimate is apparently biased. One interesting point is the increased performance of the right swath when compared to the left swath. This is due to the relationship between the azimuth angles that are used to retrieve the wind from the left swath.

IX. Conclusions

In this paper, we have derived the unbiased C–R bound for wind retrieval using scatterometer measurements. Using simple approximations, we also derived a biased C–R bound. The unbiased bound can be used as a reliable measure of wind-retrieval accuracy for almost all true wind directions. In particular, the unbiased bound is an accurate predictor of simulation results whenever the true wind direction is not azimuthally aligned with the fore or aft antenna for fan-beam scatterometers where the wind estimate is biased. The C–R bound provides a lower bound on the covariance of the estimate [4]. Thus, the C–R bound can be useful in understanding the accuracy of scatterometer-derived winds in both present and future wind scatterometers. The approximate

biased bound derived herein can produce improved results for some cases but requires more calculations and is limited by the approximations used in its derivation. The limitations are most severe for NSCAT and SeaWinds. Applying the C–R bound to different scatterometers demonstrates that wind-estimator performance is sensitive to the modeling error and to cross-track location of the wind-vector cell.

REFERENCES

[1] E. P. Attema, "The active microwave instrument on-board the ERS-1 satellite," *Proc. IEEE*, vol. 79, pp. 791–799, June 1991.

[2] C.-Y. Chi and F. K. Li, "A comparative study of several wind estimation algorithms for spaceborne scatterometers," *IEEE Trans. Geosci. Remote Sensing*, vol. 26, pp. 115–121, Mar. 1988.

[3] Cover and Thomas, *Elements of Information Theory*, New York: Wiley, 1991.

[4] L. L. Scharf, *Statistical Signal Processing: Detection, Estimation, and Time Series Analysis*. Reading, MA: Addison-Wesley, 1991.

[5] J. A. Fessler, "Moments of implicitly defined estimators (e.g., ML and MAP): Applications to transmission tomography," *Proc. Int. Conf. Acoustics, Speech, and Signal Processing*, vol. 3662, pp. 2291–2294, 1995.

[6] P. LeComte, "CMOD4 model description," Tech. Rep. ER-TN-ESA-GP-1120, Eur. Space Agency, Mar. 1993.

[7] R. E. Fischer, "Standard deviation of scatterometer measurements from space," *IEEE Trans. Geosci. Electron.*, vol. GE-10, pp. 106–113, Apr. 1972.

[8] P. E. Johnson, D. G. Long, and T. E. Oliphant, "Geophysical modeling error in wind scatterometry," *Proc. Int. Geoscience and Remote Sensing Symp.*, Lincoln, NE, May 27–31, 1996, pp. 1721–1723.

[9] D. G. Long, R. S. Collyer, R. Reed, and D. V. Arnold, "Dependence of the normalized radar cross section of water waves on Bragg wavelength—Wind speed sensitivity," *IEEE Geosci. Remote Sensing*, vol. 34, pp. 656–666, May 1996.

[10] M. H. Freilich and R. S. Dunbar, "The accuracy of NSCAT-1 vector winds: Comparisons with NDBC buoys," *J. Geophys. Res.*, vol. 104, pp. 11 499–11 514, May 1999.

[11] F. Wentz and D. Smith, "A model function for ocean normalized radar cross section at 14.6 GHZ derived from NSCAT observations," *J. Geophys. Res.*, vol. 104, 11 231–

[12] F. M. Naderi, M. H. Freilich, and D. G. Long, "Spaceborne radar measurement of wind velocity over the ocean—An overview of the NSCAT scatterometer system," *Proc. IEEE*, vol. 79, pp. 850–866, June 1991.

[13] T.E. Oliphant, "New techniques for wind scatterometry," M.S. thesis, Brigham Young Univ., Provo, UT, Aug. 1996.

[14] M. W. Spencer, C. Wu, and D. G. Long, "Tradeoffs in the design of a spaceborne scanning pencil beam scatterometer: Application to SeaWinds," *IEEE Trans. Geosci. Remote Sensing*, vol. 35, pp. 115–126, Jan. 1997.

[15] F. Wentz, S. Peteherych, and L. Thomas, "A model function for ocean radar cross sections at 14.6 GHz," *J. Geophys. Res.*, vol. 89, no. C3, pp. 3689–3704, 1984.

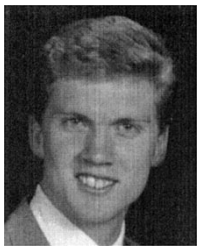

Travis E. Oliphant received the B.S. degree in electrical engineering and mathematics and the M.S. degree in electrical engineering, both from Brigham Young University (BYU), Provo, UT, in 1995 and 1996, respectively. He is currently pursuing the Ph.D. degree in biomedical engineering at the Ultrasound Research Lab, Mayo Foundation, Rochester, MN.

From 1993 to 1996, he was with the Microwave Earth Remote Sensing (MERS) Group in the Electrical and Computer Engineering Department, BYU, where he studied scatterometer-based wind estimation over water. His interests include magnetic-resonance elastography and ultrasound-stimulated vibro-acoustography, which is a novel imaging method using ultrasound radiation force.

Mr. Oliphant is the recipient of a National Science Foundation Graduate Fellowship and a Tau Beta Pi Fellowship.

David G. Long (S'80–M'82–SM'98) received the Ph.D. degree in electrical engineering from the University of Southern California, Los Angeles, in 1989.

From 1983 to 1990, he was with NASA's Jet Propulsion Laboratory (JPL), Washington, DC, where he developed advanced radar remote sensing systems. While at the JPL, he was the Senior Project Engineer on the NASA Scatterometer (NSCAT) Project. NSCAT was flown aboard the Japanese Advanced Earth Observing System (ADEOS) from 1996 to 1997. He is currently a Professor in the Electrical and Computer Engineering Department, Brigham Young University, Provo, UT, where he teaches upper division and graduate courses in communications, microwave remote sensing, radar, and signal processing. He is the principle investigator on several NASA-sponsored interdisciplinary research projects in remote sensing, including innovative radar systems, spaceborne scatterometry of the ocean and land, and modeling of atmospheric dynamics. He is a member of the NSCAT Science Working Team and has numerous publications in signal processing and radar scatterometry. His research interests include microwave remote sensing, radar theory, space-based sensing, estimation theory, computer graphics, signal processing, and mesoscale atmospheric dynamics.